In-situ synthesis of self-standing cobalt-doped nickel sulfide nanoarray as a recyclable and integrated catalyst for peroxymonosulfate activation

Liping Jiang [a], Ziyi Wei [a], Yuhan Ding [a], Yiyue Ma [a], Xue Fu [a], Jing Sun [b], Min Ma [a,*], Wenxin Zhu [a,*], Jianlong Wang [a,*]

[a] College of Food Science and Engineering, Northwest A&F University, Yangling 712100, Shaanxi, China
[b] Qinghai Provincial Key Laboratory of Qinghai-Tibet Plateau Biological Resources, Northwest Institute of Plateau Biology, Chinese Academy of Sciences, Xining 810008, Qinghai, China

ARTICLE INFO

ABSTRACT

The existing catalysts for sulfate radical-based advanced oxidation processes (SR-AOPs) are mostly in the powder form. However, the application of powdered catalyst often leads to problems such as increased cost due to difficult recovery. In this study, an in-situ synthesized self-supporting cobalt-doped nickel sulfide nanosheet array on nickel foam (NCS/NF) is proven capable of working as a recyclable and integrated catalyst for peroxymonosulfate (PMS) activation. This integrated catalyst is more practical in water treatment due to its separable and recyclable properties. In this study, a series of experiments show that the catalytic degradation performance of NCS/NF toward levofloxacin hydrochloride (LFX) could be comparable to most powdered catalysts. The catalytic mechanism analyses show that the incorporated cobalt plays a predominant role in enhancing PMS activation.

1. Introduction

Organic contaminants in wastewater are currently still a ubiquitous and serious problem worthy of widespread concern [1]. Wide-ranging using of antibiotics such as levofloxacin hydrochloride (LFX) has further exacerbated this problem [2]. Applying biological technology to treat such non-biodegradable organic wastewater is difficult to accomplish at present [3]. Tremendous efforts have been devoted to develop other advanced technologies for the remediation of organic contaminants. Advanced oxidation processes (AOPs), as a kind of environmental-friendly and efficient methods to generate reactive radicals for the elimination of recalcitrant organic pollutants, are of great significance for the treatment of such kind of wastewater [4,5].

Traditional AOPs mainly include the in-situ generation of hydroxyl radical ($\bullet OH$) with a standard redox potential of 1.8–2.7 V vs. NHE for the degradation of organic contaminants [6]. Nevertheless, $\bullet OH$ not only has an extremely short half-life of 20 ns but also is unstable in acidic condition. These characteristics limit its application in AOPs [7]. In recent years, sulfate radical ($SO_4^{\bullet-}$) based advanced oxidation process (SR-AOPs) has received more and more attention because of the high standard redox potential (2.5–3.1 V vs. NHE), long half-life time (30–40

µs), and more robust pH adaptability [7]. Generally, the common activators are categorized in these main classes: ultrasound (US), ultraviolet (UV), heat, electrocatalysis, carbon and transition metal-based catalysts [7]. Among these various activators, transition metals are often considered to be one of the most efficient alternatives. Recently, more and more studies indicate that transition metal compounds such as their oxides, hydroxides and metal-organic frameworks possess excellent PMS activation performance [8,9]. However, the use of transition-metal sulfides (TMSs) in PMS activation for organic contaminants elimination has been developed to a lesser extent [10]. In most cases, sulfide-modification has been thought to be an effective way to improve the catalytic performance via accelerating electron transfer [11]. Coincidentally, the PMS activation efficiency is closely related to the electron transfer rate of a catalyst [12,13]. In comparison with monometallic sulfides (nickel sulfide or cobalt sulfide), the catalytic contributions of Ni and Co in bimetallic sulfides could produce greater responsiveness and accelerate electron transfer, resulting in higher catalytic performance [14,15].

Homogeneous catalytic process is often considered capable of causing secondary contamination on account of the fact that dispersed transition metal ions in water environment are hard to be separated to
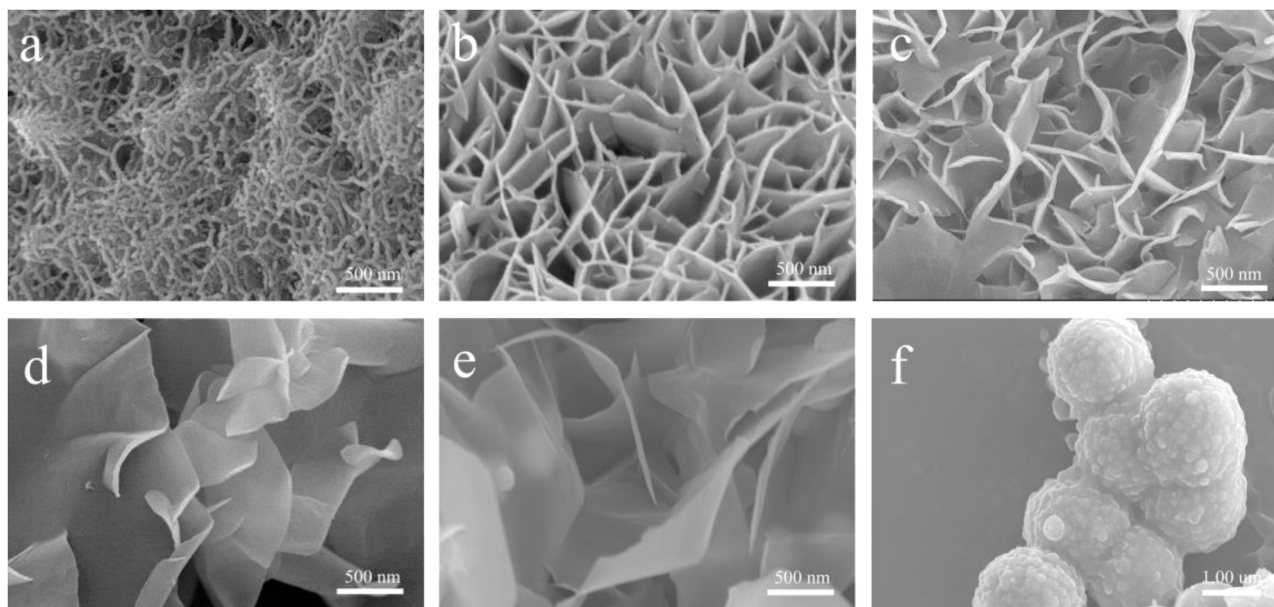

Fig. 1. SEM images of (a) NS/NF, (b) 0.6-NCS/NF, (c) 1.0-NCS/NF, (d) 1.5-NCS/NF, (e) 2.0-NCS/NF and (f) CoS$_x$.

recover. In consequence, it is an obvious tendency for researchers to develop separable and reusable heterogenous catalysts for PMS activation. At present, existing heterogeneous catalysts are mostly in powder form, which always result in a complex and time-consuming recovery process when the degradation process is finished. If this problem has not addressed, the powdered catalyst will not only adverse to the organisms and various plants in water environment, but also cause disadvantageous influences on human health [16]. Based on above-mentioned issues, we explored a chemical modification strategies of anchoring catalysts on substrates without using of binders for immobilization. Finally, we synthesized a self-supporting cobalt-doped nickel sulfide nanoarray on nickel foam (NCS/NF) using one-step hydrothermal method and explored its PMS activation efficiency [17]. On the one hand, the combination of cobalt and PMS is a valid way to enhance PMS activation efficiency [18]; On the other hand, the incorporation of cobalt may make it easier for the process of Ni(II) to Ni(III) and thus enhances the catalytic degradation efficiency of this system [19].

In order to decipher the catalytic performance of NCS/NF + PMS, a series of experiments were conducted. First, LFX was selected as a model pollutant to evaluate the catalytic performance of NCS/NF. The efficiency of NCS/NF for LFX degradation improves significantly (approximate 90% within 20 min) compared with nickel sulfide nanosheets array on NF (NS/NF) (less than 20%) and CoS$_x$ nanofilm loaded on NF (CS/NF) (approximate 70%). Then, the influences of different experimental parameters such as pH, temperature, PMS concentration and different anions in the system of NCS/NF + PMS were also studied. Furthermore, the radical quenching and electron spin resonance (ESR) analyses prove that the existed SO$_4^{\bullet-}$, $^1O_2$ and O$_2^{\bullet-}$ species in the system contribute to the degradation of LFX. The results of electrochemical tests show that NCS/NF is more prone to electron transfer, and X-ray photoelectron spectroscopy (XPS) results of fresh and used NCS/NF prove the existence of electron transfer (Ni(II)/Ni(III) and Co(II)/Co(III)) in the process of PMS activation. Following the outcome above, the largely enhanced catalytic activity of nickel sulfide is possibly attributed to that cobalt doping promotes the process of Ni(II) to Ni(III). Circulation experiment and degradation test toward other pollutants manifest that the developed system exhibits not only efficient and stable catalytic activity but also versatility to other pollutants. To sum up, the prepared NCS/NF shows excellent PMS activation ability and could realize rapid separation from pollutants after degradation.

2. Material and methods

2.1. Synthesis of NCS/NF, NS/NF and CS/NF

2.1.1. Pretreatment of NF

NF was cut into one piece with dimensions of 2.5×4 cm^2 and cleaned with HCl solution (3 M) for 5 min to remove oxide layer. Then, the pretreated NF was cleaned with distilled water.

2.1.2. Preparation of NCS/NF, NS/NF, and CS/NF

The synthesis process of NCS/NF is illustrated in Fig. S1. At first, 0.02379 g of CoCl$_2$·6H$_2$O and 0.07612 g of thiourea were dissolved into 40 mL of distilled water separately. Next, the two solutions were mixed with vigorous stirring for 30 min and then transferred into a 100 mL Teflon-lined stainless steel autoclave reactor. Finally, the pretreated NF was put into the reactor. The autoclave reactor was locked properly and placed inside a preheated oven at 120 °C for 12 h. After that, the autoclave reactor cooled down to room temperature and the prepared NCS/NF was taken out and rinsed thoroughly with distilled water. Thereafter, it was dried inside a vacuum oven at 60 °C for 12 h. NS/NF and CS/NF were synthesized in the same way as NCS/NF except the absence of CoCl$_2$·6H$_2$O or NF, and the synthesis of CoS$_x$ requires raising the temperature to 150 °C. After preparation, a catalyst suspension was prepared and loaded on to the pretreated NF to fabricate CS/NF.

Actually, we adjusted the amount of cobalt in the target materials by just changing the additional amount of CoCl$_2$·6H$_2$O in the synthesis process. The amounts of CoCl$_2$·6H$_2$O used in the process of different target products synthesis are as follows: 0.01423 g in NCS/NF-0.6, 0.02379 g in NCS/NF-1.0, 0.03569 g in NCS/NF-1.5, 0.04759 g in NCS/NF-2.0, 0.07137 g in NCS/NF-3.0, 0.09516 g in NCS/NF-4.0. The amounts of thiourea and area of nickel foam remained unchanged during the synthetic process of different target products.

2.2. Evaluation of catalytic activity

The catalytic degradation of LFX was performed under stirring (250 rpm) in a 100 mL conical flask containing LFX (10 mg L^{-1}) and PMS (0.5 mM). The reaction solution was maintained at ambient temperature unless specifically explained. The degradation process was initiated with the prepared catalyst immersing into the LFX solution. The variation of LFX concentration was measured by a UV–vis spectrophotometer
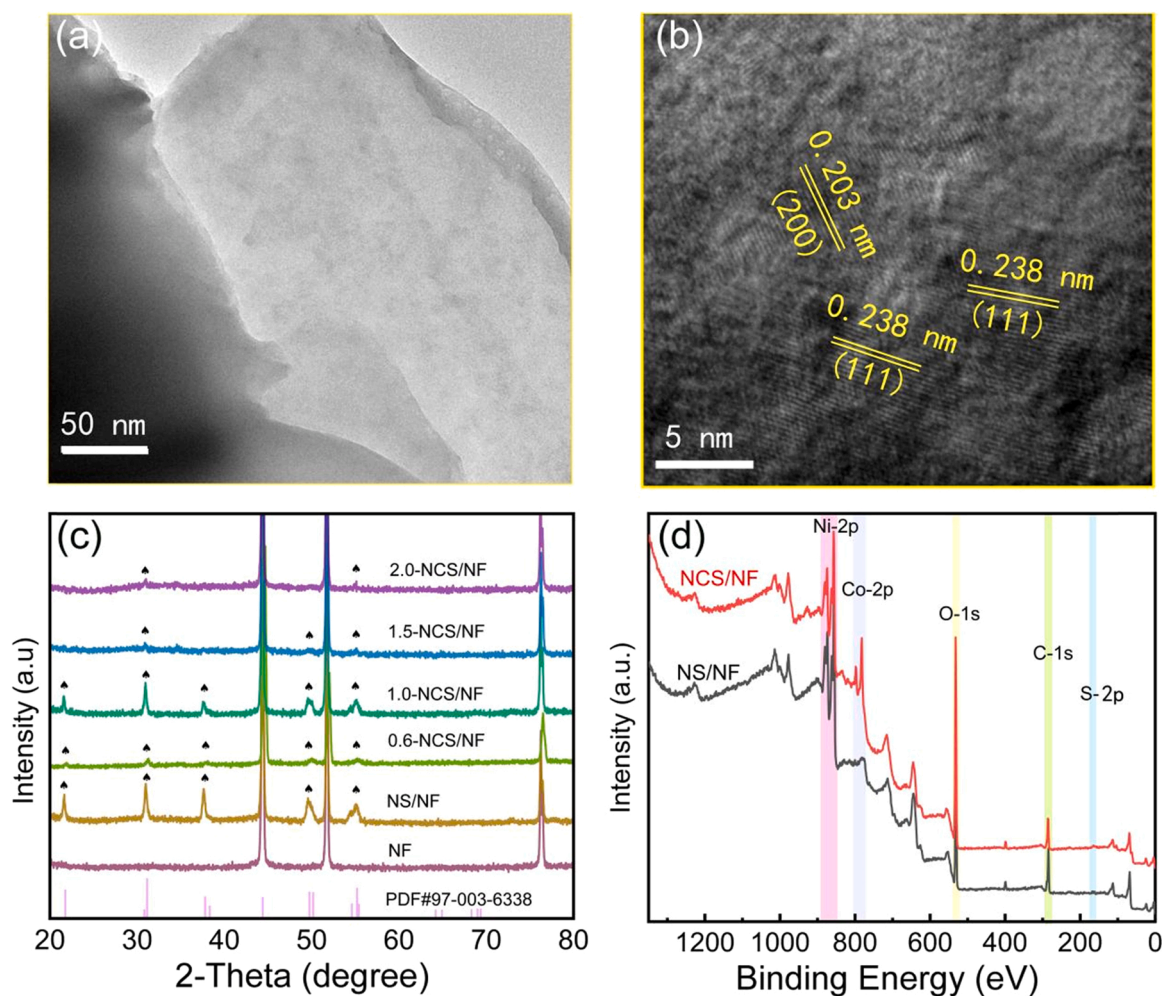
Fig. 2. (a) TEM and (b) HRTEM images of NCS; (c) XRD patterns of NF, NS/NF and NCS/NF with different Co content; (d) XPS spectra of NCS/NF and NS/NF.

(Shimadzu UV-2550) at 293 nm. If necessary, the pH value of reaction solution was adjusted by either 0.1 M $HClO_4$ or NaOH aqueous solution and recorded with a Rex pH meter (model PHS-3 C).

3. Results and discussion

### 3.1. Synthesis and characterization of NCS/NF

NCS/NF was prepared using a one-step hydrothermal method. Information about the optical images of prepared samples was provided in Fig. S2. The microstructures of the synthesized samples were characterized by SEM. It can be observed from Fig. S3 that the cleaned NF possesses 3D texture with flat and smooth surface. As shown in Fig. (1b-e), the NCS/NF catalysts with different amounts of Co are in-situ grown on the surface of NF. Moreover, the NS/NF (Fig. 1a) has a thick and unformed nanosheets network while NCS/NF (Fig. 1b-e) shows an ultrathin and independent three-dimensional structure, which could be due to that the incorporation of cobalt affects the growth of nanosheet and the nanosheet structure tends to expand with the increase of Co incorporation [20]. Furthermore, as illustrated in Fig. S4, the energy-dispersive X-ray spectroscopy (EDS) data and element mapping of NCS/NF reveal that Ni, Co and S elements are existed and uniformly distributed in the self-supporting NCS/NF nanosheets. Besides, the element content distribution shows that the content of Co is much less than Ni and S.

TEM was used to further characterize the morphology of synthesized samples (Fig. 2a). Obviously, NCS/NF has thin and stretchy nanosheet structure, which is consistent with the SEM images. Afterwards, a closer observation of NCS/NF by high-resolution TEM (HRTEM) (Fig. 2b) reveals that the lattice fringes with interplanar spacings around 0.238 and 0.203 nm correspond to the (111) and (200) crystallographic planes of Ni_3S_2, respectively. The crystalline structure and phase purity of the sample are further examined by X-ray diffraction (XRD). As shown in Fig. 2c, the typical XRD reflection peaks at 21.8°, 30.8°, 37.8°, 44.4°, 49.7° and 54.6° can be indexed to the (100), (110), (111), (200), (210) and (211) planes of Ni_3S_2 (JCPDS No. 97-003-6338), respectively. Interestingly, no peaks related to cobalt sulfide phases can be detected even when increasing the doping amount of Co. These results show that commercial NF as a nickel source was successfully vulcanized and Co atoms stabilize in a doping state in the lattice of Ni_3S_2 probably. In addition, the doping of Co could not change the crystalline phase of original Ni_3S_2 due to the similar ionic radius between Co and Ni [21,22]. Notably, when the doping amount of Co is higher than that in NCS/NF-1, the peak intensity belonging to Ni_3S_2 decreases with the increasing amount of Co, suggesting that excess Co might affect the crystallinity of Ni_3S_2.

Nitrogen adsorption-desorption isotherms (Fig. S5) show that both the NCS/NF and NS/NF exhibited similar type IV isotherms with a type H_3 hysteresis loops, suggesting the existence of mesopores in these two samples [23]. However, the BET surface area of both the two samples are small and there is no significant difference between them. Therefore, the surface area should not be the main factor affecting the catalytic performance of NCS/NF. Furthermore, XPS was used to analyze the near surface composition and valence states of NCS/NF. As shown in Fig. 2d,
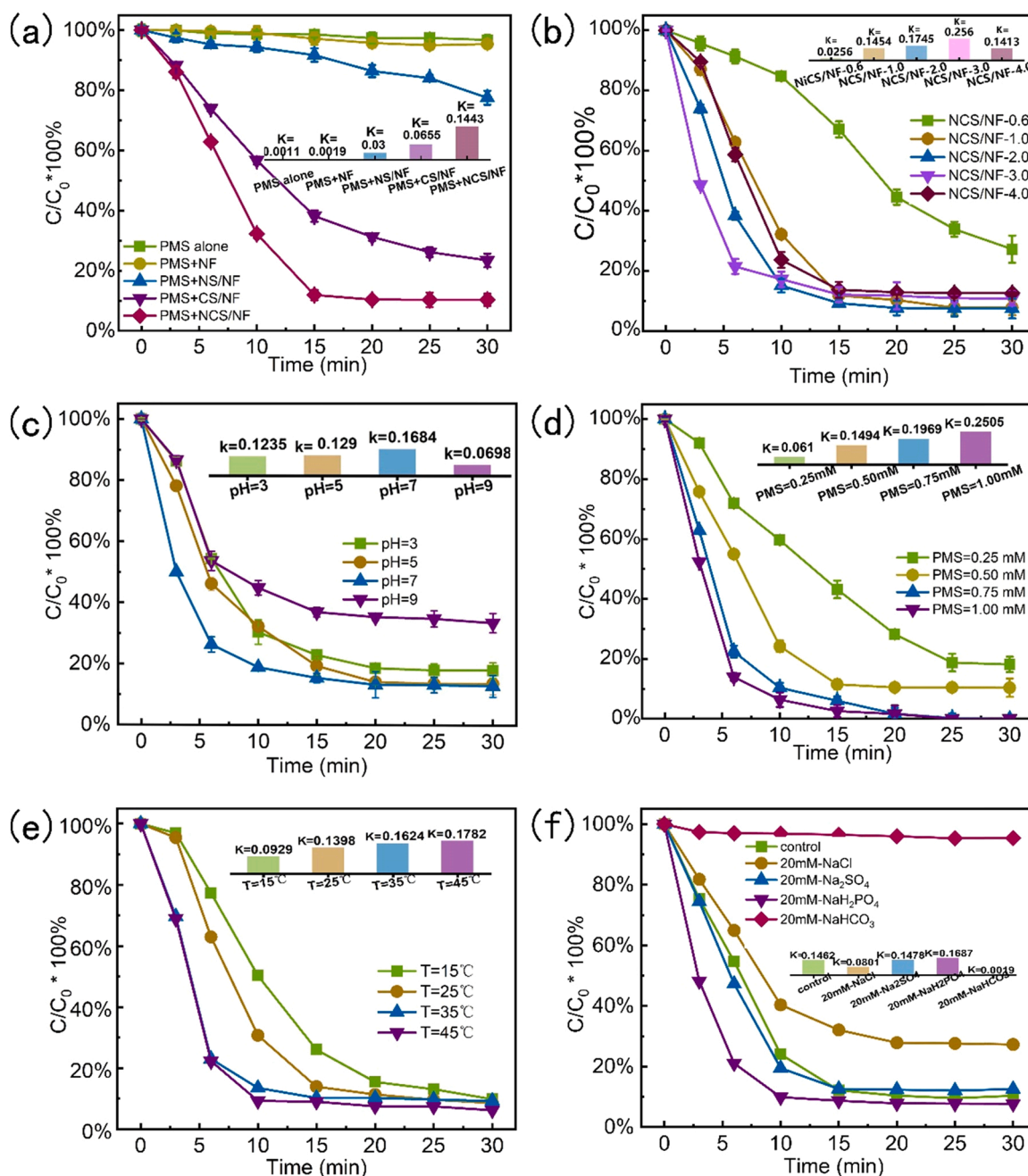
Fig. 3. (a) Degradation performance and the corresponding reaction rate constant of LFX in different systems; (b) Degradation performance and corresponding reaction rate constant of LFX degradation in the presence of different amount of doped cobalt; Effects of (c) initial pH, (d) PMS concentration, (e) temperature and (f) different anions on the degradation of LFX in the system of NCS/NF + PMS. Experimental conditions: [LFX] = 10 mg L^{-1}, [PMS] = 0.5 mM, [catalyst] = 2 × 2 cm^2.

the survey spectra demonstrate the presence of Ni, Co and S elements in the sample of NCS/NF [24]. The Ni 2p spectrum of NCS/NF depicts two main peaks located at 856.07 and 873.77 eV, which can be ascribed to Ni 2p$_{3/2}$ and Ni 2p$_{1/2}$, respectively [25,26]. Compared with the peaks of Ni 2p$_{1/2}$ and Ni 2p$_{3/2}$ in NS/NF, the slightly positive peaks shift in NCS/NF may be due to the slightly different electronegativity of Co (1.88) and Ni (1.92) [22]. In conclusion, all above characterizations prove the successful fabrication of NCS/NF.

3.2. Degradation performances of LFX in different systems

To evaluate the catalytic performance of NCS/NF for PMS activation, the degradation efficiency values of LFX in different reaction systems

were compared. The results illustrated in Fig. 3a corroborate that the removal of LFX treated by just PMS is negligible (less than 5%) due to the feeble oxidation capacity of PMS (EHSO$_5^-$/HSO$_4^-$ = 1.82 V) [7,27]. In addition, the degradation performances with catalyst alone are shown in Fig. S6, suggesting that there exists faint adsorption of LFX on the surfaces of NCS/NF, NS/NF or NF alone, which is consistent with the low surface area. However, coupling of PMS and NCS/NF (NCS/NF + PMS) leads to an excellent LFX degradation performance and approximately 90% of LFX was decomposed within 20 min, while only approximately 5%, 20% and 70% of LFX could be decomposed in the systems of NF + PMS, NS/NF + PMS and CS/NF + PMS, respectively. A pseudo-first-kinetics pattern expressed in Eq. (1) was used to fit the degradation rate constants to further investigate the catalytic behavior
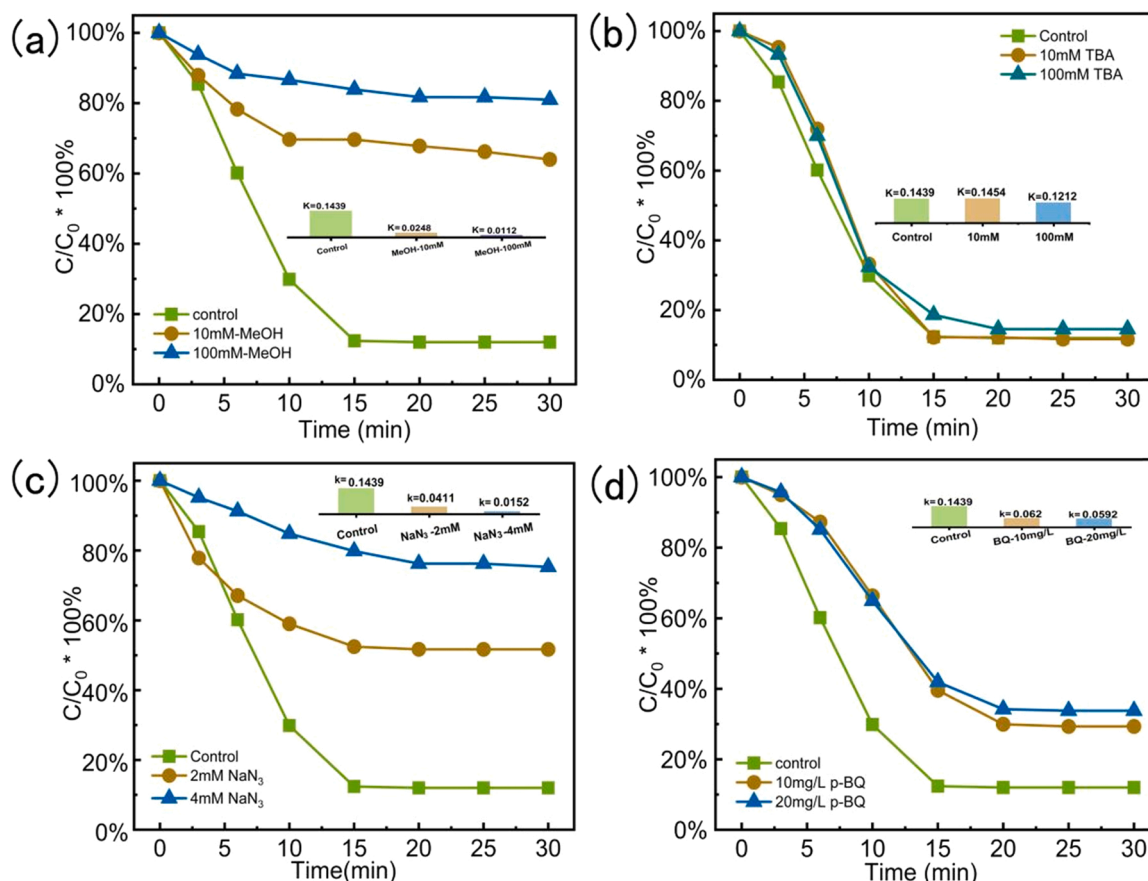
Fig. 4. Degradation performance and corresponding reaction rate constant of LFX degradation with various scavengers of (a) methanol, (b) TBA; (c) NaN₃ and (4) P-BQ. Experimental conditions: [LFX] = 10 mg L^{-1}, [PMS] = 0.5 mM, [catalyst] = 2 × 2 cm^2.

in different systems, which were calculated to be 0.1443 min^{-1} (NCS/NF + PMS), 0.0019 min^{-1} (NF + PMS), 0.03 min^{-1} (NS/NF + PMS) and 0.0655 min^{-1} (CS/NF + PMS).

$$\ln (C/C_0) = -k \cdot t \tag{1}$$

where C and C_0 represent the LFX concentration at reaction time of t = t and 0, respectively; k (min^{-1}) refers to the pseudo first order rate constant of LFX degradation; t indicates reaction time.

Furthermore, the LFX degradation performances of NCS/NF with different amounts of doped Co for PMS activation were evaluated. It can be seen from Fig. 3b that the degradation performance increases gradually with the increase of Co content in NCS/NF, which means that Co plays an important role in this catalytic process. It is noteworthy that although the Co content in NCS/NF-4.0 does not decrease significantly (Fig. S7), the catalytic performance of NCS/NF-4.0 decrease significantly compared with NCS/NF-3.0, which means that the catalytic performance is not completely related to the doping amount of Co in the catalyst. Together with the results of LFX degradation in the systems of CS/NF + PMS, NS/NF + PMS, we can speculate that there exists a synergistic effect between the doped Co and nickel sulfide in PMS activation [28].

The change of PMS concentration with the prolongation of degradation time in the system of NCS/NF + PMS was measured and presented in Fig. S9 (standard curve in Fig. S8), and the PMS concentration can reach 0.063 mM, indicating that the utilization rate of PMS in this system can reach 87.4%. In order to further show the advance of the prepared catalyst, we added a table (Table S1) and listed the related catalytic performance of similar powdered catalysts for comparison. As we can see from the table, the catalytic performance of NCS/NF is not inferior to most powdered catalysts.

3.3. LFX degradation in different conditions

3.3.1. 1 LFX degradation at different pH

In most AOPs, pH plays an important role in the elimination of organic molecule, which affects the type of ultimate radicals [29]. To understand the pH effect on the removal of LFX, 0.1 M HClO₄ or 0.1 M NaOH were employed to adjust the pH values of reaction solution. As shown in Fig. 3c, the removal rate of LFX shows a slightly increasing trend with the pH increasing from 3 to 7. However, the removal rate of LFX decreased slightly with the pH value further increasing to 9, which is in accordance with previous researches [29,30].

Generally speaking, PMS is mainly present in the form of HSO₅⁻ under slightly acidic and neutral conditions as the pKₐ = 9.4 for H₂SO₅ [18]. Hydrogen ion (H⁺) can scavenge sulfate and hydroxyl radicals to some extent according to Eqs. (2) and (3) [11,18]. These facts may be the reason why the catalytic performance improves in the pH range from acidic to neutral condition. The identified suppression at higher pH probably results from the self-decomposition of PMS to SO₄²⁻ and O₂ (Eqs. (4–6)) via a non-radical pathway suppressing the generation of SO₄•⁻ [31,32]. Additionally, OH⁻ would scavenge SO₄•⁻ and become the dominator with the increased pH value [18]. Nevertheless, •OH has a lower redox potential and shorter half-life compared with SO₄•⁻, which are detrimental for the removal of pollutants. These above results indicate that near-neutral or weakly acidic conditions are favorable for the degradation of LFX. Besides, pH plays a key role in the formation of transition metals species and their availability for reaction with oxidant= [18,33]. In addition, lower pH also affects the stability of catalyst. Evidences have shown that cobalt species are not stable under acidic conditions. Therefore, the catalyst might be leached under acidic conditions, resulting in the reduction of catalytic active sites [18].
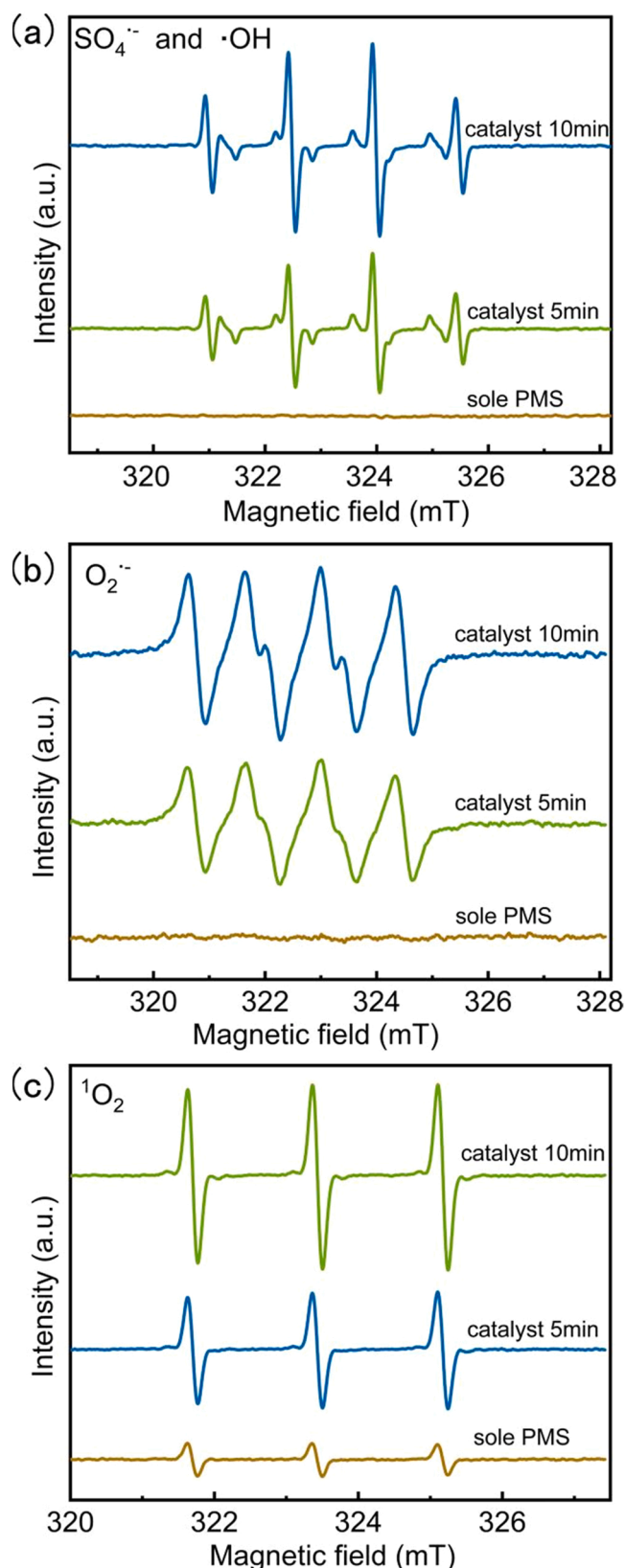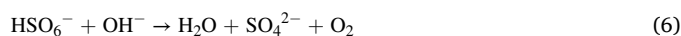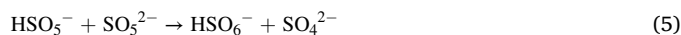
Fig. 5. ESR spectra of (a) DMPO-$SO_4^{\bullet-}$ and DMPO-$\bullet OH$, (b) TEMP-$^1O_2$ and (c) DMPO-$O_2^{\bullet-}$.

$$\bullet OH + H^+ + e^- \rightarrow H_2O \qquad (2)$$

$$SO_4^{\bullet-} + H^+ + e^- \rightarrow HSO_4^{\bullet-} \qquad (3)$$

$$HSO_5^- + H_2O \rightarrow SO_5^{2-} + H_3O^+ \qquad (4)$$

$$HSO_5^- + SO_5^{2-} \rightarrow HSO_6^- + SO_4^{2-} \qquad (5)$$

$$HSO_6^- + OH^- \rightarrow H_2O + SO_4^{2-} + O_2 \qquad (6)$$

3.3.2. LFX degradation in different PMS concentration

The effect of PMS concentration on the degradation of LFX was investigated (Fig. 3d) and the removal efficiency of LFX increases with the PMS concentration rising from 0.25 to 1.0 mM. It can be seen that the influence of PMS concentration on the catalytic degradation process is significant when the PMS concentration is lower than 0.5 mM, but the influence gradually fades away with the further increase of PMS concentration. The results could be explained that PMS has been always regarded as a reactant for the production of active species [34]. The influence of PMS concentration will be reduced with the amount of PMS in plenty relative to the pollutant. Therefore, when the amount of PMS increases to more than 0.5 mM, the catalytic performance increases indistinctively.

3.3.3. LFX degradation at different temperatures

The degradation rate of LFX is also determined in different temperatures (Fig. 3e). The catalytic reaction will accelerate with the rise of temperature and the pseudo-first order rate constants for 15, 25, 35 and 45 °C are 0.0929, 0.1398, 0.1624 and 0.1782 min^{-1}, respectively. The result suggests that the process of PMS activation by NCS/NF is endothermic, thereby, high temperature is favorable for the generation of reactive species to enhance the LFX degradation [29].

3.3.4. LFX degradation with the existence of different anions

The widespread anions in real wastewater such as HCO_3^-, $H_2PO_4^-$, SO_4^{2-} and Cl^-, could react with $SO_4^{\bullet-}/\bullet OH$ to form weaker radicals and ultimately affect the degradation efficiency of pollutants [13,18]. Therefore, the influences of widespread anions on LFX degradation are worth noting. In this study, the influences of four anions (HCO_3^-, $H_2PO_4^-$, SO_4^{2-} and Cl^-) on the degradation of LFX were studied (Fig. 3f). Firstly, Cl^- is one of the most dominant dissolved constituents in actual wastewater and representative scavenging ion affecting the availability of $SO_4^{\bullet-}$. As depicted in Fig. 3f, the obvious inhibition on LFX degradation is observed in the presence of 20 mM Cl^-. The negative effect of Cl^- can be mainly attributed to the scavenging of $SO_4^{\bullet-}$ to produce low-active chloride radical anions ($Cl\bullet$ and $Cl_2^{\bullet-}$), while the redox potentials of $Cl\bullet$ and $Cl_2^{\bullet-}$ are lower than that for $SO_4^{\bullet-}$ (2.4 eV of $Cl\bullet$, 2.0 eV of $Cl_2^{\bullet-}$, 2.5–3.1 eV of $SO_4^{\bullet-}$). [29,35]. In addition, the generated $Cl\bullet$ and $Cl_2^{\bullet-}$ will undergo a series of electron transfer reactions as shown in Eqs. (7) and (8), resulting in the consumption of reactive species and thus reducing the efficiency of pollutant degradation [36,37].

$$SO_4^{\bullet-} + Cl^- \rightarrow SO_4^{2-} + Cl\bullet \qquad (7)$$

$$\bullet OH + Cl\bullet \rightarrow ClOH\bullet^- \qquad (8)$$

Inconsiderable reduction in LFX removal rate occurs in the presence of SO_4^{2-} (20 mM) (Fig. 3f). This result suggests that SO_4^{2-} is not a robust scavenger for related ROS in this system. The degradation system is based on the transformation of $SO_4^{\bullet-}$ to SO_4^{2-}, which may be the main reason resulted in the slight inhibitory effect of SO_4^{2-} [37,38].

The degradation of LFX in the presence of $H_2PO_4^-$ (20 mM) is greatly accelerated similar to previous studies. The positive effect of $H_2PO_4^-$ might be related to the acceleration of PMS decomposition [12,37]. The nucleophiles such as $H_2PO_4^-$ are easy to attack asymmetric structure (PMS) and accelerate the production of radicals, leading to the rapid
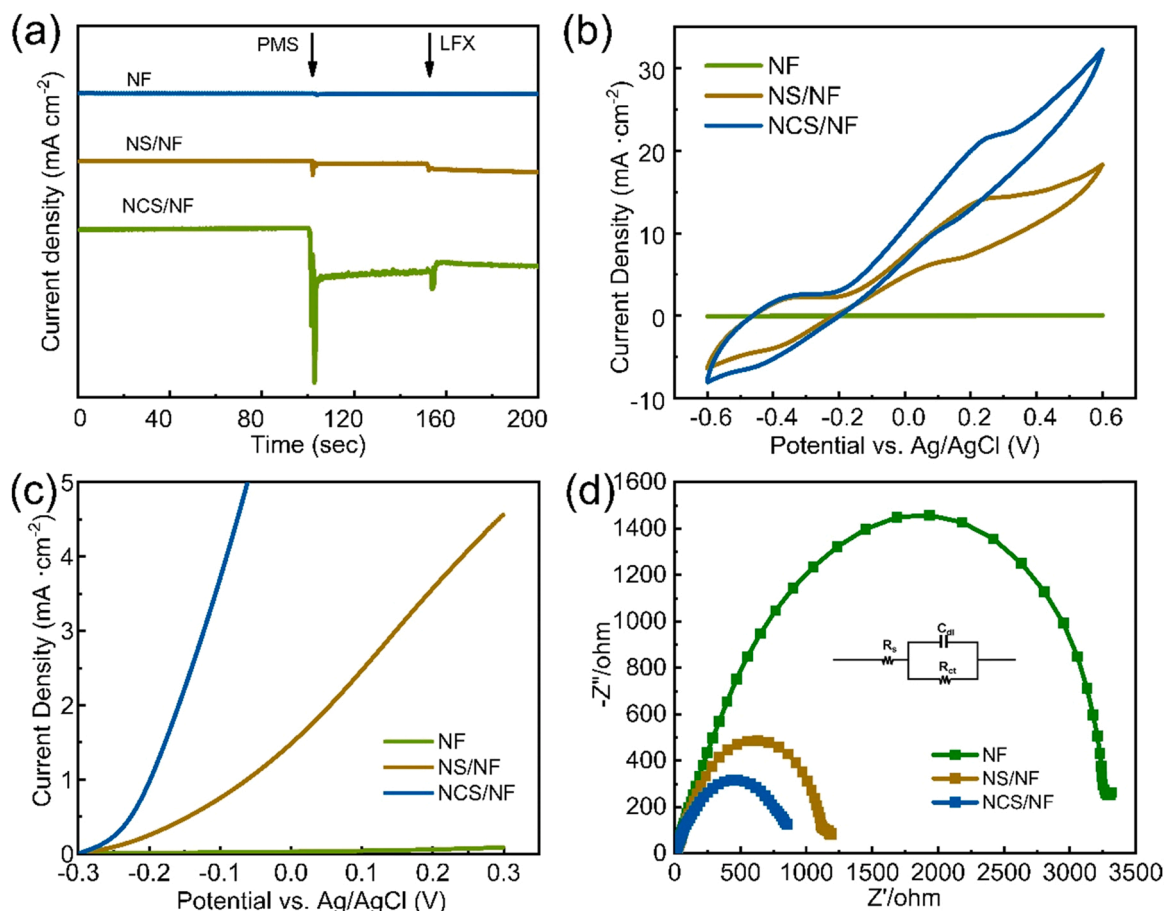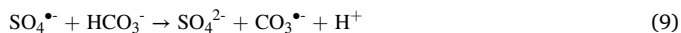
Fig. 6. (a) The i-t curves of different catalysts obtained at open circuit potential vs. Ag/AgCl using 0.05 M Na$_2$SO$_4$ as electrolyte; (b) CV curves of different catalysts at a scan rate of 50 mV s^{-1} (0.5 M Na$_2$SO$_4$); (c) LSV curves of different catalysts (0.05 M Na$_2$SO$_4$); (d) Nyquist plots of different catalysts (0.5 M Na$_2$SO$_4$).

degradation of LFX by more reactive groups such as O$_2^{\bullet-}$ and SO$_4^{\bullet-}$ eventually [12,37,39].

Obviously, an evident inhibition could be observed with the addition of 20 mM HCO$_3^-$ in the degradation system. Only less 10% of LFX were degraded within 20 min in the presence of 20 mM HCO$_3^-$. Previous studies have proven that HCO$_3^-$ can directly compete SO$_4^{\bullet-}$, •OH and O$_2^{\bullet-}$ with LFX to generate CO$_3^{\bullet-}$ with a lower redox potential (E$_0$ = 1.78 V vs NHE), and the corresponding reactions are shown in Eqs. (9) and (10) [37,40].

$$SO_4^{\bullet-} + HCO_3^- \rightarrow SO_4^{2-} + CO_3^{\bullet-} + H^+ \qquad (9)$$

$$\bullet OH + HCO_3^- \rightarrow H_2O + CO_3^{\bullet-} \qquad (10)$$

3.4. Identification of reactive species in NCS/NF + PMS system

Quenching experiments were conducted to identify the kinds of radicals in the reaction system directly [37]. Firstly, methanol was employed as a scavenger for both •OH and SO$_4^{\bullet-}$ due to its second-order rate constants (k) with SO$_4^{\bullet-}$ of 3.2 × 10^6 M^{-1} s^{-1} and •OH of 9.7 × 10^8 M^{-1} s^{-1} [41]. The degradation is obviously inhibited when methanol is appeared in the system (Fig. 4a), which means both SO$_4^{\bullet-}$ and •OH could be the contributing factors for the degradation of LFX. Tert-butyl alcohol (TBA) as a scavenger shows good affinity to •OH (k = 3.8–7.6 × 10^8 M^{-1} s^{-1}). The inhibitory effect of TBA for the degradation of LFX is negligible, indicating that NCS/NF activates PMS to produce SO$_4^{\bullet-}$ rather than •OH (Fig. 4b) [41]. NaN$_3$ and p-BQ are effective quenching agents of singlet oxygen (^{1}O$_2$) and superoxide anion radical (O$_2^{\bullet-}$),

respectively. When NaN$_3$ was added into the system, an apparent quenching effect can be observed (Fig. 4c). This result indicates that ^{1}O$_2$ plays important role in the degradation of LFX. At the same time, it is worth noting that the quenching effect of p-BQ on the degradation of LFX was obviously weaker than that of NaN$_3$ (Fig. 4d), indicating that O$_2^{\bullet-}$ is not the only precursor for the generation of ^{1}O$_2$ in the NCS/NF + PMS system [42]. Based on above mentioned issues, SO$_4^{\bullet-}$, ^{1}O$_2$ and O$_2^{\bullet-}$ can work together for the efficient decomposition of LFX in the system of NCS/NF + PMS and the contribution of O$_2^{\bullet-}$ is relatively weak.

To further prove the production of dominant reactive groups in the NCS/NF + PMS system. In-situ electron spin resonance (ESR) analysis was also utilized to probe the formation and evolution of radicals during LFX degradation. As can be seen from Fig. 5a-c, there is no characteristic signals appeared in the separate PMS system except for TEMP-^{1}O$_2$. However, obvious signals of DMPO-•OH (1:2:2:1 triplet signals), DMPO-SO$_4^{\bullet-}$ (lower intensity peaks between hydroxyl radicals' characteristic peaks), TEMP-^{1}O$_2$ (1:1:1 triplet signals) and DMPO-O$_2^{\bullet-}$ (1:1:1:1 triplet signals) were observed in the system of NCS/NF + PMS [43]. The intensities of these signals increase with the extension of catalytic reaction time. The signal intensities of •OH are much higher than those for SO$_4^{\bullet-}$ which is in contrary to the results of quenching experiments, This phenomenon should be due to the rapid change of DMPOC-SO$_4^{\bullet-}$ to DMPOC-•OH [19,44]. Generally speaking, the production of SO$_4^{\bullet-}$, •OH and O$_2^{\bullet-}$ indicates that the degradation process is caused by free radical pathways, while the presence of ^{1}O$_2$ indicates that non-free radical pathway also exists in this system for the degradation of LFX [7,45].
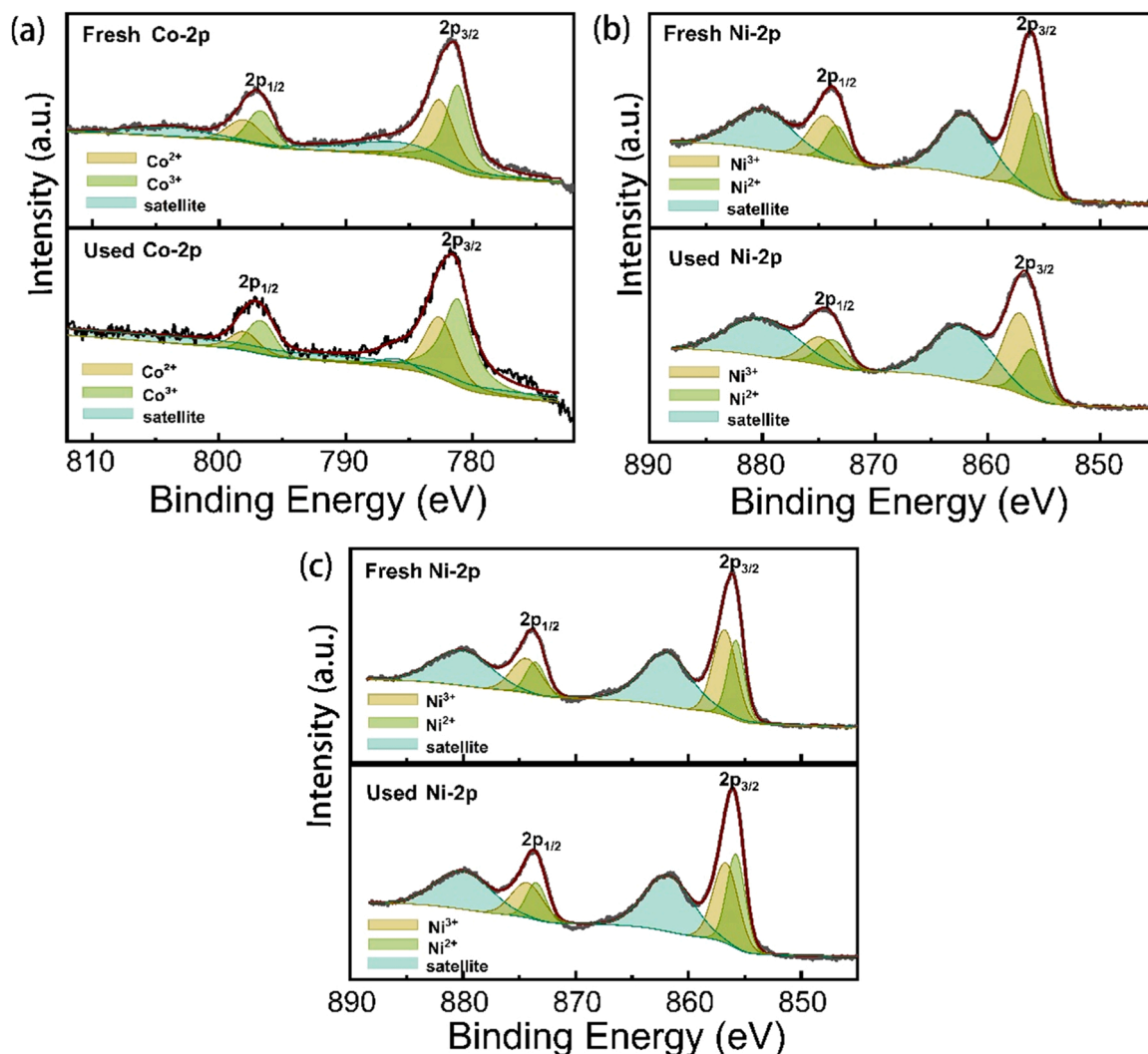
Fig. 7. High-resolution XPS spectra in the regions of (a) Co-2p and (b) Ni-2p for fresh and used NCS/NF; (c) High-resolution Ni-2p spectra for fresh and used NS/NF.

3.5. Possible degradation mechanism

As previously reported that the process of PMS activation to produce radicals is essentially related to the charge transport efficiency [48]. Herein, electrochemical measurements were conducted to demonstrate the electrons transfer in the process of PMS activation. As depicted in Fig. 6a, the current density dropped obviously when PMS contacts with NCS/NF, while for NS/NF and NF, the current density shows tiny changes. The sudden change in current density probably resulted from an instantaneous electron motion between the surface of NCS/NF and PMS molecules [13,23]. Subsequently, the addition of LFX also leads to an obvious change in current density just for NCS/NF, implying that the transfer of electrons takes place between LFX molecules and catalyst [23,46]. The cyclic voltammetry (CV) curves of NCS/NF, NS/NF and NF are displayed in Fig. 6b. Compared with NS/NF and NF, NCS/NF exhibits the highest current density and most evident redox capability coordinating the redox process [12,47,48], which may be related to the easier electron transferof Ni sites after Co doping. The results of linear sweep voltammetry (LSV) curves (Fig. 6c) also show a higher current density for NCS/NF in comparison with NS/NF and NF, which indicates a faster electron conduction of NCS/NF [12]. Furthermore, the obtained Nyquist plots show NCS/NF has the lowest charge transfer resistance value compared with other samples, also indicating that NCS/NF is more prone to electron transfer (Fig. 6d) [23,49].

Based on this result, the XPS survey spectra of NCS/NF before and

after reaction were depicted in Fig. 7a-c and the related peaks data are shown in Table S2–4. As shown in Table S2 and Fig. 7a, it is found that the chemical valence state of Co(II) species decreased from 46.27% to 38.42% after reaction and Ni(II) species decreased slightly from 38.7% to 36.8%. There is no obvious peak shift occurs on Co site. The result means that the partial electron transfer of Co(II) to Co(III) occurs on the surface of NCS/NF accompanied by the electron transfer from catalyst to PMS (Eq. (11)) [13,50]. Significantly, the main peaks of Ni 2p slightly shifted ~0.35 eV to higher binding energies after reaction, indicating that the specific change in valence states occurs on nickel site. In order to further explore the valence state change of nickel, herein, the XPS spectra of fresh and used NS/NF were investigated. As shown in Fig. 7c, the chemical valence state of Ni(II) does not decrease in NS/NF, which means the charge transfer of Ni(II) to Ni(III) accompanied by the electron transfer from catalyst to PMS does not occur in the system of NS/NF+PMS but occur in the system of NCS/NF+PMS during PMS activation (Eq. (12)) [10]. Compared with NS/NF, we speculate that the incorporated Co in NCS/NF makes it easier from Ni(II) to Ni(III). According to previous studies, some reaction pathways may also exist in this system. For example, Co(III) and Ni(III) might be reduced by PMS with the generation of $SO_5^{\bullet-}$ (Eqs. (13–14)) [37,51]. In addition, Co(III) and Ni(III) might be reduced to Co(II) and Ni(II) via oxidation reduction cycle of S_2^{2-}/S^{2-} to other sulfate species on the surface of NCS/NF (Eqs. (15,16)) [11]. This conjecture can be verified in Fig. S10 that the S-2p XPS spectrum changed obviously before and after reaction. Based on
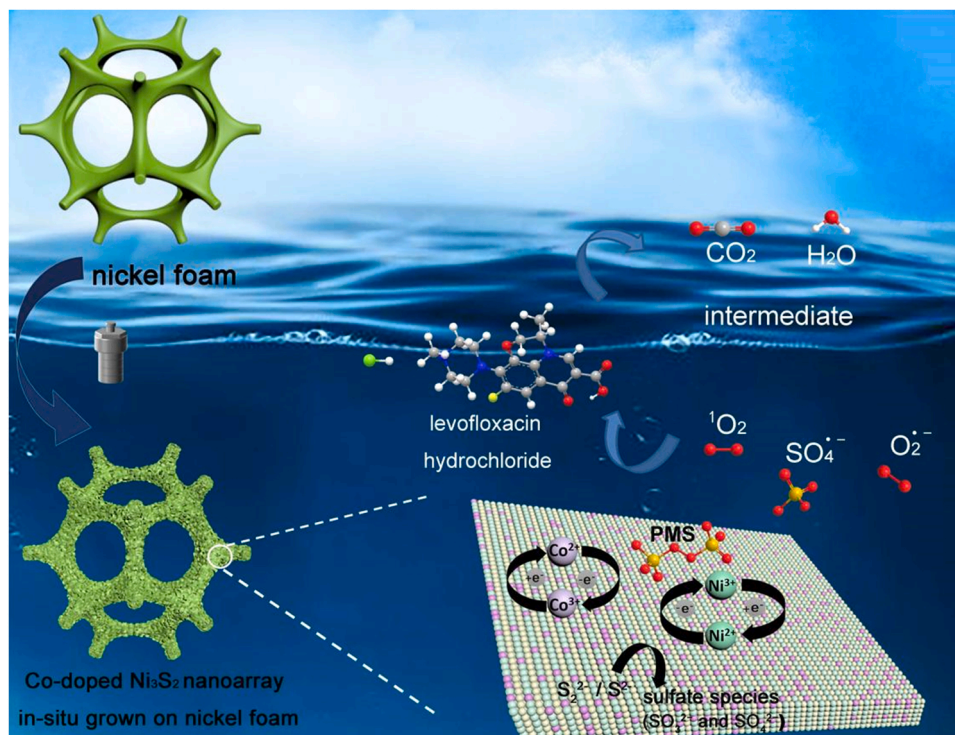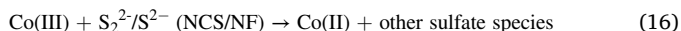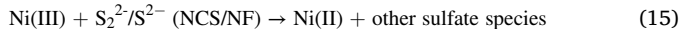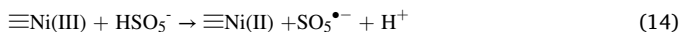
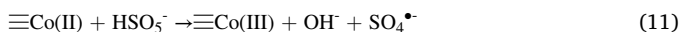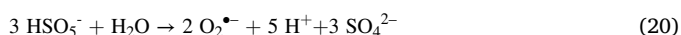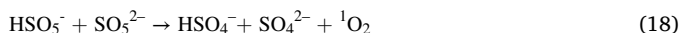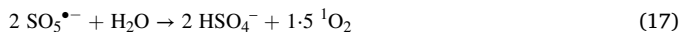**Fig. 8.** Proposed mechanism of LFX decomposition in the system of NCS/NF+PMS.

above discussion and previous research, the degradation mechanism in the system of NCS/NF + PMS is well understood. To sum up, as shown in Fig. 8, doping Co into nickel sulfide provides more active sites and enhances the process of Ni(II) to Ni(III), which may be the reason why the PMS activation efficiency of NCS/NF is much higher than those for NS/NF and CS/NF.

$$\equiv Co(II) + HSO_5^- \rightarrow \equiv Co(III) + OH^- + SO_4^{\bullet-} \quad (11)$$

$$\equiv Ni(II) + HSO_5^- \rightarrow \equiv Ni(III) + OH^- + SO_4^{\bullet-} \quad (12)$$

$$\equiv Co(III) + HSO_5^- \rightarrow \equiv Co(II) + SO_5^{\bullet-} + H^+ \quad (13)$$

$$\equiv Ni(III) + HSO_5^- \rightarrow \equiv Ni(II) + SO_5^{\bullet-} + H^+ \quad (14)$$

$$Ni(III) + S_2^{2-}/S^{2-} (NCS/NF) \rightarrow Ni(II) + \text{other sulfate species} \quad (15)$$

$$Co(III) + S_2^{2-}/S^{2-} (NCS/NF) \rightarrow Co(II) + \text{other sulfate species} \quad (16)$$
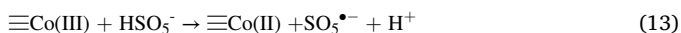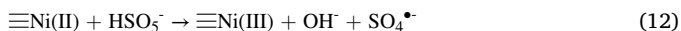
As shown in Fig. 5c, characteristic signals of TEMP-$^1O_2$ (1:1:1 triplet signals) appears in the separate PMS system indicating that the $^1O_2$ can be produced by the self-decomposition of PMS. Combined with previous literatures on PMS activation by transition-metal sulfides, the generation of $^1O_2$ might be attributed to both the production of $SO_5^{\bullet-}$ and self-decomposition of PMS (Eqs. (17,18)). According to the results of EPR and radical quenching experiments, only a small amount of $O_2^{\bullet-}$ is formed in the system of NCS/NF + PMS. This result means $O_2^{\bullet-}$ might be created concomitantly by the electron transfer between $SO_5^{\bullet-}$ and dissolved oxygen or the self-decomposition of PMS (Eqs. (19)-(20)) [28].

$$2 SO_5^{\bullet-} + H_2O \rightarrow 2 HSO_4^- + 1.5\ ^1O_2 \quad (17)$$

$$HSO_5^- + SO_5^{2-} \rightarrow HSO_4^- + SO_4^{2-} + {}^1O_2 \quad (18)$$

$$SO_4^{\bullet-} + O_2 \rightarrow O_2^{\bullet-} + SO_4^{2-} \quad (19)$$

$$3 HSO_5^- + H_2O \rightarrow 2 O_2^{\bullet-} + 5 H^+ + 3 SO_4^{2-} \quad (20)$$

3.6. Degradation test toward other pollutants

In order to evaluate the versatility of the NCS/NF + PMS system, the degradation performances towards other four pollutants including rhodamine B (RB), methylene blue (MB), tetracycline (TC), methyl green (MG) were further evaluated. As shown in Fig. S11, the catalytic behaviors in the system of NCS/NF + PMS on the degradation of various pollutants are different. The removal efficiencies within 15 min of RB, MB, TC and MG over NCS/NF + PMS are 100%, 95.22%, 86.4% and 83.11%, respectively, and the reaction rate constants are estimated to be 0.6718, 0.2027, 0.1376 and 0.1163 min^{-1}, respectively. This result suggests that the NCS/NF + PMS system shows universal applicability and favorable catalytic performance towards a variety of pollutants.

3.7. Possible degradation pathway of LFX

The representative UV–vis spectra of reaction system as a function of oxidation time are illustrated in Fig. S12 to explore the mineralization processes of LFX. After treated for 15 min, the absorbance at around 293 nm reduced significantly, indicative of the destruction of characteristic chromophore in LFX molecule. The absorbance peaks located at 225 and 256 nm corresponded to the conjugated double bond and benzene of LFX, which decrease with the prolongation of degradation time. Besides, TOC (total organic carbon) and TC (total carban) test is used to evaluate the mineralization of LFX. As shown in Fig. S13, the decrease of TOC/TC was not obvious in the initial 30 min and turns to be apparent after 30 min. Combined with the representative UV–vis spectra of the reaction system, we can conclude that the destruction of characteristic chromophore (LFX) mainly occurred in the first 30 min and the mineralization of the pollutant mainly occurred after 30 min. The final TOC removal efficiency rate of the system can reach 43.32% after 120 min. Based on the above mentioned, the degradation process may be accompanied by the mineralization of LFX (Eq. 21) [38].

$$LFX + PMS \rightarrow \text{intermediate} \rightarrow CO_2 + H_2O + SO_4^{2-} \quad (21)$$
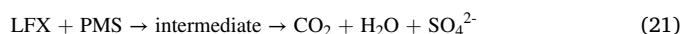
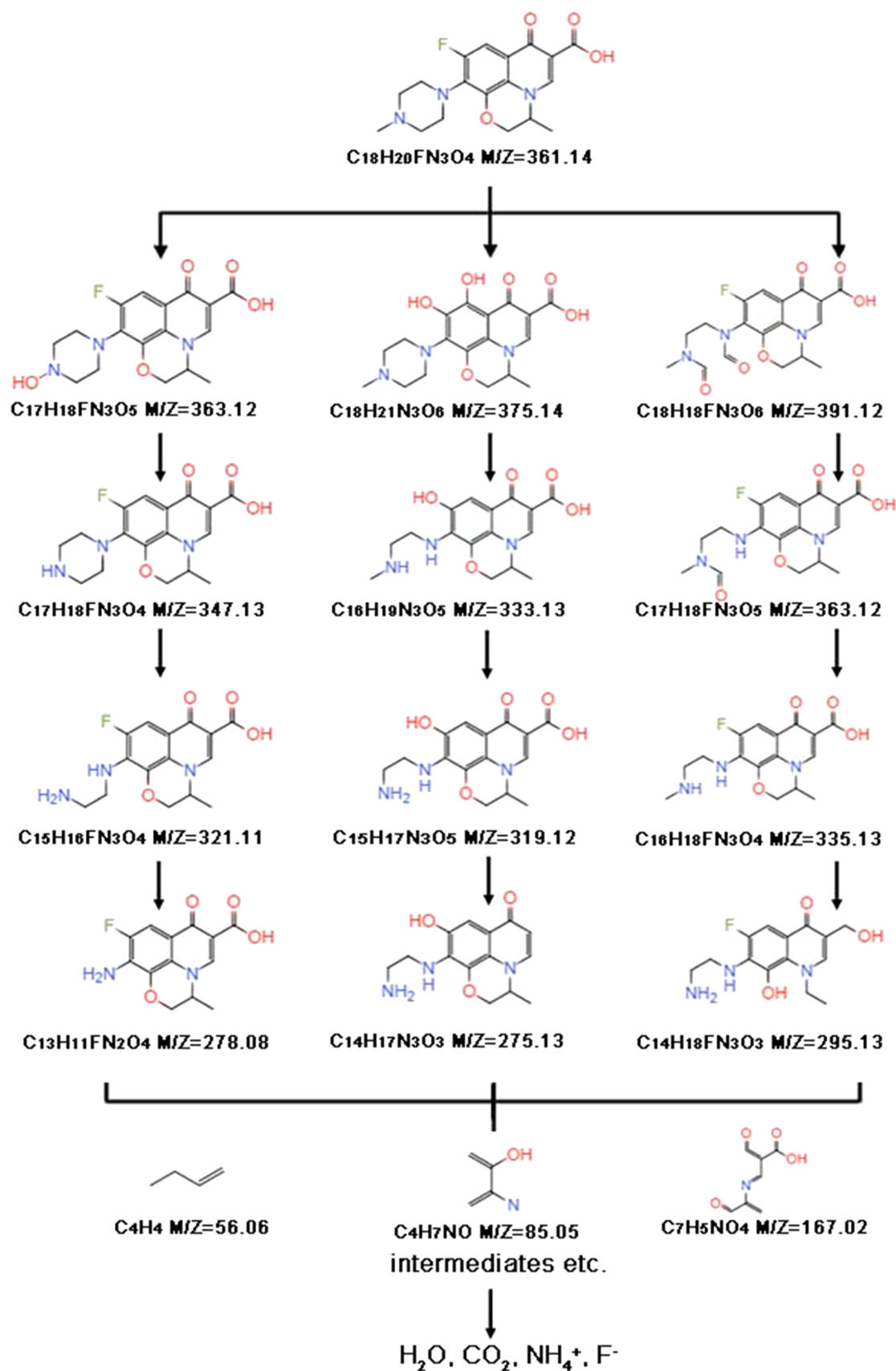In order to better understand the degradation pathway of LFX, we

Fig. 9. The possible degradation pathways of LFX in the system of NCS/NF+PMS.

detected the primary intermediates by UHPLC/HRMS in positive ion mode. We have detected 16 intermediates and summarized their corresponding molecular formula, m/z values, molecular structure and retention times in Table S6. All MS spectra of the possible intermediates are displayed in Fig. S14.

Based on reported studies and the analysis results of obtained intermediates, the possible LFX degradation pathways are proposed as illustrated in Fig. 9. Due to the attack of ROS, a series of reactions such as de-hydroxylation, de-methylation, de-carboxylation, de-fluorination and ring opening could occurr in the degradation system [52]. For example, in the pathway I, LFX (P_1) ($m/z = 361.14$) is converted to P_2 ($m/z = 363.12$) by replacing methyl group on LFX parent ion with hydroxyl group [53]. Then, P_3 ($m/z = 347.13$) is obtained by de-hydroxylation reaction. Subsequently, the ring of P_3 could be destroyed by ROS, leading to the formation of P_4 ($m/z = 321.11$) and P_5 ($m/z = 278.08$) [54]. In the pathway II, P_6 ($m/z = 375.14$) is formed by the substitution of fluorine on P_1 ($m/z = 361.14$) [55]. P_7 ($m/z = 333.14$) is obtained by de-hydroxylation and ring open reactions of P_6 [51,52]. P_8 ($m/z = 319.12$) is formed by de-methylation reaction of P_7. Ultimately, P_9 ($m/z = 275.13$) is obtained by de-carboxylation reactions of P_8. In the pathway III, the generation of P_{10} ($m/z = 391.12$), P_{11} ($m/z = 363.12$) may be attributed to the destruction of piperazine ring [54]. In this process, P_{12} ($m/z = 335.13$) and P_{13} ($m/z = 295.13$) are also produced through de-hydroxylation and de-methylation [51]. In addition, the generation of P_{14}, P_{15} and P_{16} means that the complete structure of quinolinic moiety in the products would also be destroyed, which are eventually mineralized to CO_2, H_2O, F^-, NH_4^+, etc [51].

In order to explore the stability of this catalysts, SEM, XRD and XPS data of NCS/NF after reaction were recorded firstly. As shown in the SEM image (Fig. S15), the catalyst sustain well its nanosheets array structure. The change in phase was further analyzed by XRD analysis. As shown in Fig. S16, the corresponding diffraction peak positions of the catalysts after reaction were almost unchanged while their peak intensities decreased to some extent. In addition, there is no obvious change in the XPS survey spectra of NCS/NF before and after reaction (Fig. S17). Atomic absorption spectrophotometer was used to detect the leaching of Co and Ni during reaction (Fig. S18). The result shows that slight leaching of Co (below 0.1 ppm) was detected during reaction comparing with Ni ions (below 1.0 ppm). The reusability of catalyst is of great significance for the practical application in realistic conditions, thus, the recycling experiment was further conducted. The result in Fig. S19 shows that the LFX degradation efficiency within 20 min is declined from ~90% (in the first cycle) to ~70% (in the second cycle) and there is only a slight decrease until the sixth cycle. The reduction in catalytic capacity may be due to the adsorption of degradation products on the catalyst surface and the loss of surface sites.

4. Conclusions

In conclusion, a self-supporting cobalt-doped nickel sulfide nanosheet array in-situ grown on nickel foam (NCS/NF) was found to be capable of working as a recyclable and integrated catalyst for PMS activation. When using the NCS/NF to activate PMS to degrade LFX, the degradation efficiency could be up to approximately 90% within 20 min. Remarkably, the used NCS/NF can be separated directly from water environment without centrifugation, making it more practical than powdered catalyst in actual application. The radical quenching and ESR experiments confirm that $SO_4^{\bullet-}$, $^1O_2$ and $O_2^{\bullet-}$ radicals act as the active species in the system of NCS/NF + PMS. The doped Co in NCS/NF makes Ni(II) easier to convert to Ni(III) and the redox circles of Ni(II)/Ni(III) and Co(II)/Co(III) are jointly responsible for PMS activation. Circulation experiment and the degradation test toward other pollutants manifest that this NCS/NF + PMS system exhibits not only robust catalytic degradation ability toward LFX, but also high versatility to other pollutants. In short, this work provides a promising integrated PMS catalyst for environmental remediation.

References

[1] F. Wania, D. Mackay, Peer reviewed: tracking the distribution of persistent organic pollutants, Environ. Sci. Technol. 30 (1996) 390A–396A.
[2] Y. Zhao, X. Yuan, L. Jiang, X. Li, J. Zhang, H. Wang, Reutilization of cathode material from spent batteries as a heterogeneous catalyst to remove antibiotics in wastewater via peroxymonosulfate activation, Chem. Eng. J. 400 (2020), 125903.
[3] R. Ramachandran, T. Sakthivel, M. Li, H. Shan, Z.-X. Xu, F. Wang, Efficient degradation of organic dye using Ni-MOF derived NiCo-LDH as peroxymonosulfate activator, Chemosphere 271 (2021) 128509.
[4] C.A. Martínez-Huitle, M.A. Rodrigo, I. Sirés, O. Scialdone, Single and coupled electrochemical processes and reactors for the abatement of organic water pollutants: a critical review, Chem. Rev. 115 (2015) 13362–13407.
[5] W.D. Oh, G. Lisak, R.D. Webster, Y.N. Liang, A. Veksha, A. Giannis, J.G.S. Moo, J. W. Lim, T.T. Lim, Insights into the thermolytic transformation of lignocellulosic biomass waste to redox-active carbocatalyst: durability of surface active sites, Appl. Catal. B 233 (2018) 120–129.
[6] C. Wang, J. Kim, V. Malgras, J. Na, J. Lin, J. You, M. Zhang, J. Li, Y. Yamauchi, Metal–organic frameworks and their derived materials: emerging catalysts for a sulfate radicals-based advanced oxidation process in water purification, Small 15 (16) (2019), 1900744.
[7] M. Kohantorabi, G. Moussavi, S. Giannakis, A review of the innovations in metal- and carbon-based catalysts explored for heterogeneous peroxymonosulfate (PMS) activation, with focus on radical vs. non-radical degradation pathways of organic contaminants, Chem. Eng. J. 411 (2021) 127957.
[8] L. Kong, G. Fang, X. Xi, Y. Wen, Y. Chen, M. Xie, F. Zhu, D. Zhou, J. Zhan, A novel peroxymonosulfate activation process by periclase for efficient singlet oxygen-mediated degradation of organic pollutants, Chem. Eng. J. 403 (2021) 126445.
[9] C. Zhu, S. Zhao, Z. Fan, H. Wu, F. Liu, Z. Chen, A. Li, Confinement of CoP nanoparticles in nitrogen-doped yolk-shell porous carbon polyhedron for ultrafast catalytic oxidation, Adv. Funct. Mater. 30 (2020), 2003947.
[10] H. Jiang, C. Zhu, Y. Yuan, C. Yue, C. Ling, F. Liu, A. Li, Enhanced activation of peroxymonosulfate with metal-substituted hollow $M_xCo_{3-x}S_4$ polyhedrons for superfast degradation of sulfamethazine, Chem. Eng. J. 384 (2020) 123302.

[11] H. Zeng, L. Deng, H. Zhang, C. Zhou, Z. Shi, Development of oxygen vacancies enriched CoAl hydroxide @ hydroxysulfide hollow flowers for peroxymonosulfate activation: a highly efficient singlet oxygen-dominated oxidation process for sulfamethoxazole degradation, J. Hazard. Mater. 400 (2020), 123297.

[12] W. Du, Q. Zhang, Y. Shang, W. Wang, Q. Li, Q. Yue, B. Gao, X. Xu, Sulfate saturated biosorbent-derived Co-S @ NC nanoarchitecture as an efficient catalyst for peroxymonosulfate activation, Appl. Catal. B 262 (2020), 118302.

[13] L. Peng, Y. Shang, B. Gao, X. Xu, Co₃O₄ anchored in N, S heteroatom co-doped porous carbons for degradation of organic contaminant: role of pyridinic N-Co binding and high tolerance of chloride, Appl. Catal. B 282 (2021), 119484.

[14] J. Yang, C. Yu, X. Fan, S. Liang, S. Li, H. Huang, Z. Ling, C. Hao, J. Qiu, Electroactive edge site-enriched nickel–cobalt sulfide into graphene frameworks for high-performance asymmetric supercapacitors, Energy Environ. Sci. 9 (2016) 1299–1307.

[15] L. Yu, L. Zhang, H.B. Wu, X.W. Lou, Formation of NiₓCo₃₋ₓS₄ hollow nanoprisms with enhanced pseudocapacitive properties, Angew. Chem. Int. Ed. 126 (2014) 3785–3788.

[16] H. Yan, R. Wang, R. Liu, T. Xu, J. Sun, L. Liu, J. Wang, Recyclable and reusable direct Z-scheme heterojunction CeO₂/TiO₂ nanotube arrays for photocatalytic water disinfection, Appl. Catal. B 291 (2021), 120096.

[17] L. Zhu, J. Ji, J. Liu, S. Mine, M. Matsuoka, J. Zhang, M. Xing, Designing 3D-MoS₂ sponge as excellent cocatalysts in advanced oxidation processes for pollutant control, Angew. Chem. Int. Ed. 59 (2020) 13968–13976.

[18] P. Hu, M. Long, Cobalt-catalyzed sulfate radical-based advanced oxidation: a review on heterogeneous catalysts and applications, Appl. Catal. B 181 (2016) 103–117.

[19] Z.Y. Guo, C.X. Li, M. Gao, X. Han, Y.J. Zhang, W.J. Zhang, W.W. Li, Mn-O covalency governs the intrinsic activity of Co-Mn spinel oxides for boosted peroxymonosulfate activation, Angew. Chem. Int. Ed. 60 (2021) 274–280.

[20] S. Xie, J. Gou, B. Liu, C. Liu, Synthesis of cobalt-doped nickel sulfide nanomaterials with rich edge sites as high-performance supercapacitor electrode materials, Inorg. Chem. Front. 5 (2018) 1218–1225.

[21] J.G. Wang, R. Zhou, D. Jin, K. Xie, B. Wei, Controlled synthesis of NiCo₂S₄ nanostructures on nickel foams for high-performance supercapacitors, Energy Storage Mater. 2 (2016) 1–7.

[22] G. Zhang, Y.S. Feng, W.T. Lu, D. He, C.Y. Wang, Y.K. Li, X.Y. Wang, F.F. Cao, Enhanced catalysis of electrochemical overall water splitting in alkaline media by Fe doping in Ni3S2 nanosheet arrays, ACS Catal. 8 (2018) 5431–5441.

[23] M. Wang, Y. Cui, H. Cao, P. Wei, C. Chen, X. Li, J. Xu, G. Sheng, Activating peroxydisulfate with Co₃O₄/NiCo₂O₄ double-shelled nanocages to selectively degrade bisphenol A-A nonradical oxidation process, Appl. Catal. B 282 (2021), 119585.

[24] W. Kong, C. Lu, W. Zhang, J. Pu, Z. Wang, Homogeneous core–shell NiCo₂S₄ nanostructures supported on nickel foam for supercapacitors, J. Mater. Chem. A 3 (2015) 12452–12460.

[25] P. Chen, T. Zhou, M. Zhang, Y. Tong, C. Zhong, N. Zhang, L. Zhang, C. Wu, Y. Xie, 3D nitrogen-anion-decorated nickel sulfides for highly efficient overall water splitting, Adv. Mater. 29 (2017), 1701584.

[26] Q. Xu, H. Jiang, H. Zhang, Y. Hu, C. Li, Heterogeneous interface engineered atomic configuration on ultrathin Ni (OH) 2/Ni₃S₂ nanoforests for efficient water splitting, Appl. Catal. B 242 (2019) 60–66.

[27] Y. Fan, Z. Zhou, Y. Feng, Y. Zhou, L. Wen, K. Shih, Degradation mechanisms of ofloxacin and cefazolin using peroxymonosulfate activated by reduced graphene oxide-CoFe₂O₄ composites, Chem. Eng. J. 383 (2020), 123056.

[28] J. Zhang, W. Zhao, S. Wu, R. Yin, M. Zhu, Surface dual redox cycles of Mn (III)/Mn (IV) and Cu (I)/Cu (II) for heterogeneous peroxymonosulfate activation to degrade diclofenac: performance, mechanism and toxicity assessment, J. Hazard. Mater. 410 (2021), 124623.

[29] R. Yuan, M. Jiang, S. Gao, Z. Wang, H. Wang, G. Boczkaj, Z. Liu, J. Ma, Z. Li, 3D mesoporous α-Co (OH)₂ nanosheets electrodeposited on nickel foam: a new generation of macroscopic cobalt-based hybrid for peroxymonosulfate activation, Chem. Eng. J. 380 (2020), 122447.

[30] S.-F. Jiang, L.-L. Ling, W.-J. Chen, W.-J. Liu, D.-C. Li, H. Jiang, High efficient removal of bisphenol A in a peroxymonosulfate/iron functionalized biochar system: mechanistic elucidation and quantification of the contributors, Chem. Eng. J. 359 (2019) 572–583.

[31] Z. Wu, Y. Wang, Z. Xiong, Z. Ao, S. Pu, G. Yao, B. Lai, Core-shell magnetic Fe₃O₄ @ Zn/Co-ZIFs to activate peroxymonosulfate for highly efficient degradation of carbamazepine, Appl. Catal. B 277 (15) (2020) 119136.

[32] J. Sun, X. Li, J. Feng, X. Tian, Oxone/Co²⁺ oxidation as an advanced oxidation process: comparison with traditional Fenton oxidation for treatment of landfill leachate, Water Res. 43 (2009) 4363–4369.

[33] F. Ghanbari, M. Moradi, Application of peroxymonosulfate and its activation methods for degradation of environmental organic pollutants, Chem. Eng. J. 310 (2017) 41–62.

[34] L.-X. Yang, J.-C.E. Yang, M.-L. Fu, Magnetic CoFe₂O₄ nanocrystals derived from MIL-101 (Fe/Co) for peroxymonosulfate activation toward degradation of chloramphenicol, Chemosphere 272 (2021), 129567.

[35] X. Zhou, A. Jawad, M. Luo, C. Luo, T. Zhang, H. Wang, J. Wang, S. Wang, Z. Chen, Z. Chen, Regulating activation pathway of Cu/persulfate through the incorporation of unreducible metal oxides: pivotal role of surface oxygen vacancies, Appl. Catal. B 286 (2021), 119914.

[36] W. Li, S. Li, Y. Tang, X. Yang, W. Zhang, X. Zhang, H. Chai, Y. Huang, Highly efficient activation of peroxymonosulfate by cobalt sulfide hollow nanospheres for fast ciprofloxacin degradation, J. Hazard. Mater. 389 (2020), 121856.

[37] X. Dong, B. Ren, X. Zhang, X. Liu, Z. Sun, C. Li, Y. Tan, S. Yang, S. Zheng, D. Dionysiou, Diatomite supported hierarchical 2D CoNi₃O₄ nanoribbons as highly efficient peroxymonosulfate catalyst for atrazine degradation, Appl. Catal. B 272 (2020), 118971.

[38] R. Yuan, J. Jiang, Z. Wang, S. Gao, Z. Liu, M. Li, G. Boczkaj, Hierarchical MnO₂ nanoflowers blooming on 3D nickel foam: a novel micro-macro catalyst for peroxymonosulfate activation, J. Colloid Interface Sci. 571 (2020) 142–154.

[39] C. Li, Y. Huang, X. Dong, Z. Sun, X. Duan, B. Ren, S. Zheng, D.D. Dionysiou, Highly efficient activation of peroxymonosulfate by natural negatively-charged kaolinite with abundant hydroxyl groups for the degradation of atrazine, Appl. Catal. B 247 (2019) 10–23.

[40] Y. Huang, X. Li, C. Zhang, M. Dai, Z. Zhang, Y. Xi, B. Quan, S. Lu, Y. Liu, Degrading arsanilic acid and adsorbing the released inorganic arsenic simultaneously in aqueous media with CuFe₂O₄ activating peroxymonosulfate system: factors, performance, and mechanism, Chem. Eng. J. 424 (2021), 128537.

[41] Y.H. Guan, J. Ma, X.C. Li, J.Y. Fang, L.W. Chen, Influence of pH on the formation of sulfate and hydroxyl radicals in the UV/peroxymonosulfate system, Environ. Sci. Technol. 45 (2011) 9308–9314.

[42] L. Luo, Z. Su, J. Zhuo, L. Huang, Y. Nian, L. Su, W. Zhang, J. Wang, Copper-sensitized "Turn On" peroxidase-like activity of MMoO₄ (M= Co, Ni) flowers for selective detection of aquatic copper Ions, ACS Sustain. Chem. Eng. 8 (2020) 12568–12576.

[43] A. Wang, Y. Chen, Z. Zheng, H. Wang, X. Li, Z. Yang, R. Qiu, K. Yan, In situ N-doped carbon-coated mulberry-like cobalt manganese oxide boosting for visible light driving photocatalytic degradation of pharmaceutical pollutants, Chem. Eng. J. 411 (2021), 128497.

[44] G.S. Timmins, K.J. Liu, E.J. Bechara, Y. Kotake, H.M. Swartz, Trapping of free radicals with direct in vivo EPR detection: a comparison of 5, 5-dimethyl-1-pyrroline-N-oxide and 5-diethoxyphosphoryl-5-methyl-1-pyrroline-N-oxide as spin traps for HO and SO₄•⁻, Free Radic. Biol. Med. 27 (1999) 329–333.

[45] W.D. Oh, Z. Dong, T.T. Lim, Generation of sulfate radical through heterogeneous catalysis for organic contaminants removal: current development, challenges and prospects, Appl. Catal. B 194 (2016) 169–201.

[46] Y.-Y. Ahn, H. Bae, H.-I. Kim, S.-H. Kim, J.-H. Kim, S.-G. Lee, J. Lee, Surface-loaded metal nanoparticles for peroxymonosulfate activation: efficiency and mechanism reconnaissance, Appl. Catal. B 241 (2019) 561–569.

[47] W. Li, Z. Wang, H. Liao, X. Liu, L. Zhou, Y. Lan, J Zhang, Enhanced degradation of 2, 4, 6-trichlorophenol by activated peroxymonosulfate with sulfur doped copper manganese bimetallic oxides, Chem. Eng. J. (2020), 128121.

[48] X. Duan, C. Su, J. Miao, Y. Zhong, Z. Shao, S. Wang, H. Sun, Insights into perovskite-catalyzed peroxymonosulfate activation: maneuverable cobalt sites for promoted evolution of sulfate radicals, Appl. Catal. B 220 (2018) 626–634.

[49] Y. Liu, J. Luo, L. Tang, C. Feng, J. Wang, Y. Deng, H. Liu, J. Yu, H. Feng, J. Wang, Origin of the enhanced reusability and electron transfer of the carbon-coated Mn₃O₄ nanocube for persulfate activation, ACS Catal. 10 (2020) 14857–14870.

[50] H. Xu, D. Wang, J. Ma, T. Zhang, X. Lu, Z. Chen, A superior active and stable spinel sulfide for catalytic peroxymonosulfate oxidation of bisphenol S, Appl. Catal. B 238 (2018) 557–567.

[51] Y. Pang, J. Zhou, X. Yang, Y. Lan, C. Chen, Rationally designed Co₃O₄-SnO₂ activated peroxymonosulfate for the elimination of chloramphenicol, Chem. Eng. J. 418 (2021), 129401.

[52] Z. He, W. Zheng, M. Li, W. Liu, Y. Zhang, Y. Wang, Fe₂P/biocarbon composite derived from a phosphorus-containing biomass for levofloxacin removal through peroxymonosulfate activation, Chem. Eng. J. 427 (2022), 130928.

[53] J. Zhou, W. Liu, W. Cai, The synergistic effect of Ag/AgCl @ ZIF-8 modified g-C3N4 composite and peroxymonosulfate for the enhanced visible-light photocatalytic degradation of levofloxacin, Sci. Total Environ. 696 (2019), 133962.

[54] S. Li, C. Wang, M. Cai, F. Yang, Y. Liu, J. Chen, P. Zhang, X. Li, X. Chen, Facile fabrication of TaON/Bi₂MoO₆ core–shell S-scheme heterojunction nanofibers for boosting visible-light catalytic levofloxacin degradation and Cr (VI) reduction, Chem. Eng. J. 428 (2022), 131158.

[55] X.J. Wen, C.G. Niu, H. Guo, L. Zhang, C. Liang, G.M. Zeng, Photocatalytic degradation of levofloxacin by ternary Ag₂CO₃/CeO₂/AgBr photocatalyst under visible-light irradiation: degradation pathways, mineralization ability, and an accelerated interfacial charge transfer process study, J. Catal. 358 (2018) 211–223.